

# Granular aluminium nanojunction fluxonium qubit

D. Rieger<sup>1,4</sup>✉, S. Günzler<sup>1,2,4</sup>, M. Spiecker<sup>1</sup>, P. Paluch<sup>1,2</sup>, P. Winkel<sup>1,2</sup>,  
L. Hahn<sup>3</sup>, J. K. Hohmann<sup>3</sup>, A. Bacher<sup>3</sup>, W. Wernsdorfer<sup>1,2</sup> & I. M. Pop<sup>1,2</sup>✉

Mesoscopic Josephson junctions, consisting of overlapping superconducting electrodes separated by a nanometre-thin oxide layer, provide a precious source of nonlinearity for superconducting quantum circuits. Here we show that in a fluxonium qubit, the role of the Josephson junction can also be played by a lithographically defined, self-structured granular aluminium nanojunction: a superconductor–insulator–superconductor Josephson junction obtained in a single-layer, zero-angle evaporation. The measured spectrum of the resulting qubit, which we nickname gralmonium, is indistinguishable from that of a standard fluxonium. Remarkably, the lack of a mesoscopic parallel plate capacitor gives rise to an intrinsically large granular aluminium nanojunction charging energy in the range of tens of gigahertz, comparable to its Josephson energy. We measure coherence times in the microsecond range and we observe spontaneous jumps of the value of the Josephson energy on timescales from milliseconds to days, which offers a powerful diagnostics tool for microscopic defects in superconducting materials.

The remarkable progress of superconducting quantum information processing in academia<sup>1–5</sup> and in industry<sup>6–9</sup> is fuelled by the Josephson effect<sup>10</sup>, which provides nonlinearity while maintaining coherence. In practice, the vast majority of Josephson junctions (JJs) are implemented in the form of Al–AlO<sub>x</sub>–Al superconductor–insulator–superconductor (SIS) weak links, which offer a long list of benefits, such as high control over the insulating barrier<sup>11</sup>, robustness to thermal cycling<sup>12</sup> and unmatched coherence<sup>12–14</sup>. However, due to the involved multilayer and often multi-angle evaporation processes, it is difficult to reduce the footprint of such mesoscopic SIS JJs substantially below 100 × 100 nm<sup>2</sup>. As a consequence, their critical current is suppressed in a Fraunhofer pattern for magnetic fields in the 10<sup>2</sup> mT range<sup>15</sup>, which are interesting for hybrid architectures<sup>16,17</sup>. In addition, the parallel plate electrodes of the JJ entail an unavoidable capacitance, which, if removed, could lift one of the constraints in engineering Hamiltonians with large quantum phase fluctuations<sup>3,18,19</sup>.

Other types of weak links can be used to overcome some of these limitations. For example, devices using superconductor–semiconductor–superconductor junctions<sup>20,21</sup> provide a promising

quantum information platform and have been demonstrated to be resilient to magnetic field<sup>22</sup>, but they introduce additional complexity in the fabrication process and additional noise sources due to the required gate bias. Alternatively, defining a constriction in a superconducting wire to form an ScS JJ harvests nonlinearity directly from a continuous superconducting film<sup>23,24</sup>. While ScS JJs are well established in direct current devices operated in a magnetic field<sup>25</sup>, embedding them in qubits made of homogeneously disordered superconductors<sup>26,27</sup> currently yields orders of magnitude higher dissipation compared to SIS JJ qubits<sup>8,13,18,28,29</sup>.

In this Article, we combine the advantageous coherence of SIS JJs with the nanoscopic, single-layer design of ScS JJs by using the self-structured aluminium grain assembly of granular aluminium (grAl)<sup>30,31</sup> to form a nanojunction. To assess the nonlinearity and coherence of the grAl nanojunction, we incorporate it into a fluxonium superconducting qubit, which we nickname gralmonium. Notably, this allows for a single-layer fabrication of the whole circuit, since all circuit elements for the qubit and read-out can be engineered by tailoring

<sup>1</sup>Physikalisches Institut, Karlsruhe Institute of Technology, Karlsruhe, Germany. <sup>2</sup>Institute for Quantum Materials and Technologies, Karlsruhe Institute of Technology, Eggenstein-Leopoldshafen, Germany. <sup>3</sup>Institute of Microstructure Technology, Karlsruhe Institute of Technology, Eggenstein-Leopoldshafen, Germany. <sup>4</sup>These authors contributed equally: D. Rieger and S. Günzler. ✉e-mail: [dennis.rieger@kit.edu](mailto:dennis.rieger@kit.edu); [ioan.pop@kit.edu](mailto:ioan.pop@kit.edu)

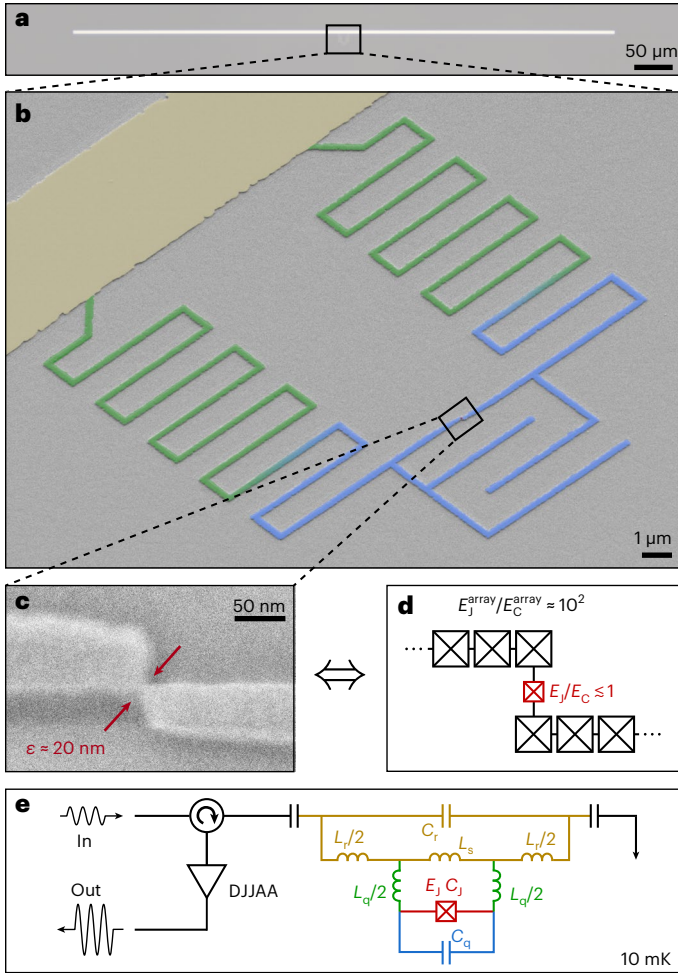


**Fig. 1 | The gralmonium, a single-layer grAl fluxonium circuit.** **a**, Optical microscope image of the antenna, serving as the read-out resonator for the gralmonium qubit located in the centre. **b**, False-coloured scanning electron microscope image of a zoomed-in view of the qubit circuit, which consists of a meandered grAl superinductor loop<sup>28</sup> (green), coupled galvanically to the antenna (ochre) and closed by a coplanar capacitor (blue) in parallel with the grAl nanojunction. **c**, Zoomed-in view of the grAl nanojunction (red arrows) implemented by an  $\varepsilon^3$  grAl volume, where  $\varepsilon \approx 20$  nm. **d**, Effective one-dimensional JJ array circuit model of the grAl nanojunction connected to the superinductor. **e**, Lumped element circuit schematic of the gralmonium qubit inductively coupled to the read-out antenna. The colours of the nanojunction, shunt capacitor  $C_q$ , superinductor  $L_q$ , resonator capacitor  $C_r$ , inductor  $L_r$ , and shared inductor  $L_s$  correspond to the highlighted colours in **b**. The read-out resonator is measured in single-port reflection using a dimer Josephson junction array amplifier (DJJAA)<sup>38</sup>.

only the geometry of the wires. We demonstrate that the gralmonium follows the standard fluxonium Hamiltonian and measure energy relaxation and coherence times on the order of 10  $\mu$ s, comparable to many superconducting qubits based on conventional SIS JJs. Moreover, the magnetic field resilience of grAl<sup>32</sup> and the nanoscopic footprint of the grAl nanojunction make the gralmonium an attractive platform for prospective applications in hybrid quantum architectures. The high susceptibility of the nanojunction to the grAl microstructure is passed on to the gralmonium and could be harnessed in future detector circuits.

Figure 1 shows the grAl nanojunction embedded into the gralmonium circuit, and the corresponding circuit model. We pattern the read-out resonator stripline antenna (Fig. 1a) and the gralmonium

located in its centre (Fig. 1b) from a 20-nm-thick grAl film with sheet resistance  $1.5 \text{ k}\Omega \square^{-1}$  on a sapphire substrate (compare with Methods). The 170-nm-wide meandered superinductance wire shares 8  $\mu$ m with the antenna, coupling the qubit to the read-out similarly to one in the literature<sup>33</sup>. The flux loop is closed by constricting the wire to an  $\varepsilon^3$  grAl volume, with  $\varepsilon = 20$  nm: the grAl nanojunction (Fig. 1c). Considering the  $\sim 4$  nm size of the grains in grAl<sup>30</sup> and the coherence length of our grAl film,  $5 \text{ nm} < \xi < 10 \text{ nm} < \varepsilon$  (refs. <sup>34,35</sup>), the nanojunction is composed of a three-dimensional network of JJs. However, for frequencies well below the plasma frequency ( $\sim 70$  GHz (refs. <sup>36,37</sup>)), the nanojunction and the connecting wire can be modelled as an effective one-dimensional array of SIS JJs<sup>36</sup> with abruptly modulated Josephson coupling (Fig. 1d). Although it is possible that several successive  $\text{AlO}_x$ -Al interfaces contribute to the nanojunction's Josephson coupling, we use a single, effective Josephson energy  $E_J$  and capacitance  $C_J$  to model the nanojunction as a zero-dimensional SIS JJ with a sinusoidal current-phase relation<sup>24</sup>.

In contrast to the superinductor JJs in which the ratio of Josephson energy to charging energy is  $E_J^{\text{array}}/E_C^{\text{array}} \approx 10^2$ , the nanojunction operates in the opposite regime of  $E_J/E_C \lesssim 1$  due to its decreased Josephson coupling and small intrinsic capacitance  $C_J < 1$  fF. To engineer the total charging energy of the gralmonium to  $E_C^{\Sigma} \approx E_J$ , we add a coplanar capacitor  $C_q$  (highlighted in blue in Fig. 1b,e) in parallel to the nanojunction. Due to the compact geometry of the gralmonium loop, some of the meanders in the vicinity of the junction also contribute to  $C_q$ , as illustrated in Fig. 1b by the colour gradient from blue to green. We model the entire circuit using an effective lumped element representation, depicted in Fig. 1e. The sample is mounted in a subwavelength copper tube (Supplementary Section I and the literature<sup>32</sup>) and measured in single-port microwave reflection employing a parametric quantum amplifier<sup>38</sup>.

The first indication of a functioning qubit coupled to the resonator is the measurement of avoided level crossings versus external flux (Fig. 2a), which repeat periodically (Supplementary Section II). By measuring the spectroscopy of the gralmonium (Fig. 2), we confirm that it is accurately modelled by the standard fluxonium Hamiltonian<sup>3</sup>:

$$H = 4E_C^{\Sigma} n^2 + \frac{1}{2} E_L \left( \varphi - 2\pi \frac{\Phi_{\text{ext}}}{\Phi_0} \right)^2 - E_J \cos \varphi, \quad (1)$$

with the grAl nanojunction serving as an SIS JJ with sinusoidal current-phase relation and effective Josephson energy  $E_J$  (compare with Fig. 1d). The operators  $n$  and  $\varphi$  correspond to the number of Cooper pairs and the phase difference across the junction, respectively;  $\Phi_0 = h/2e$  is the superconducting magnetic flux quantum, where  $h$  is Planck's constant and  $e$  is the charge of an electron;  $E_L = (\Phi_0/2\pi)^2/L_q$  is the inductive energy of the superinductor  $L_q$ ; and  $\Phi_{\text{ext}}$  is the external flux through the gralmonium loop. We quantify the agreement between the gralmonium spectrum and a sinusoidal current-phase relation in Supplementary Section IV. In total, we measured 20 spectra of gralmonium devices consistent with the fluxonium Hamiltonian (compare with equation (1)) across 11 wafers (compare with Supplementary Section X).

Figure 2b shows a gralmonium spectrum up to 14 GHz, measured by probing the read-out resonator while applying a second microwave tone varying in frequency. A joint numerical fit<sup>39</sup> of equation (1) to the  $|g\rangle \rightarrow |e\rangle$  (red) and  $|g\rangle \rightarrow |f\rangle$  (blue) transitions matches the data and gives  $E_J = 23.4$  GHz, in agreement with the expected range for the dimension of the grAl nanojunction<sup>40,41</sup>. The fitted capacitance across the junction  $C_{\Sigma} = C_q + C_J$  is 1.26 fF. The  $|g\rangle \rightarrow |f\rangle$  transition is suppressed around zero flux (Fig. 2b, top left inset), following the fluxonium selection rules<sup>3</sup>. Additionally, due to large quantum fluctuations facilitated by the small value of the nanojunction capacitance, even at zero flux, the  $|g\rangle$  and  $|e\rangle$  eigenfunctions of the gralmonium are delocalized (compare with Supplementary Section V). Surprisingly, the  $|g\rangle \rightarrow |e\rangle$  transition linewidth does not narrow as the flux bias is tuned towards the sweet spots,

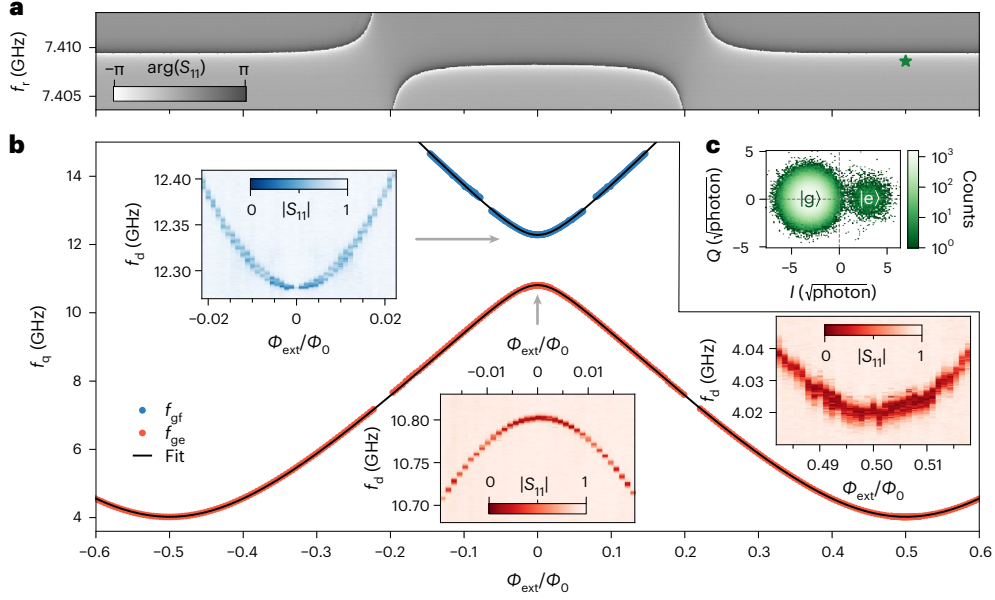


**Fig. 2 | Gralmonium spectroscopy versus external flux. a**, Read-out resonator phase response  $\arg(S_{11}(f_r))$  measured in reflection. The field sweep reveals avoided level crossings between the qubit and the resonator. **b**, Gralmonium spectrum measured by two-tone spectroscopy. The data for the  $|g\rangle \rightarrow |e\rangle$  (red markers,  $f_{ge}$ ) and  $|g\rangle \rightarrow |f\rangle$  (blue markers,  $f_{gf}$ ) transitions are extracted from continuous wave monitoring of the resonator while applying a second drive tone at  $f_d$ . The gaps in the extracted qubit frequencies  $f_q$  around 7.4 GHz and 13.1 GHz result from avoided level crossings with the read-out resonator and the first superconductor mode, respectively. From a fit to the spectrum (black lines), we extract  $L_q = 285$  nH,  $E_J/h = 23, 4$  GHz and  $C_x = C_q + C_j = 1.26$  fF ( $E_C^x/h = 15$  GHz) for the qubit parameters (compare with Fig. 1). The insets show raw spectroscopy

data at the sweet spots with the colour scale corresponding to the single-port reflection amplitude. At half-flux (bottom right inset), the qubit frequency toggles from trace to trace (on a timescale of minutes). Note that the visibility of the  $|g\rangle \rightarrow |f\rangle$  transition vanishes in the vicinity of  $\Phi_{\text{ext}} = 0$  (top left inset), as expected from the fluxonium selection rules<sup>13</sup>. **c**, The  $I$ - $Q$  histogram of contiguous reflection coefficient measurements at  $\Phi_{\text{ext}}/\Phi_0 = 0.5$  and  $f_r = 7.4086$  GHz (green marker in **a**). Each point is integrated for 784 ns at  $\bar{n} \approx 10$  circulating photons in the read-out resonator. Both  $|g\rangle$  and  $|e\rangle$  states are visible, separated by a dispersive shift  $\chi/2\pi = -1.7$  MHz (also Supplementary Section III), and their populations correspond to 37 mK effective temperature.

foreshadowing the presence of an additional decoherence mechanism besides flux noise, namely, critical current fluctuations. On a timescale of a few traces (minutes), a toggling of the half-flux frequency is observed (bottom right inset), which will be discussed in more detail in Fig. 3. In Fig. 2c we plot an  $I$ - $Q$  histogram of the measured reflection coefficient at half-flux bias, where  $I$  and  $Q$  are the in-phase and quadrature signals, respectively. The two distributions visible in the plot correspond to the steady state populations of  $|g\rangle$  and  $|e\rangle$ .

We complete the gralmonium characterization with time domain measurements at half-flux. The top row of Fig. 3 shows free decay energy relaxation and spin Hahn echo measurements with single exponential decay times on the order of 10  $\mu$ s. The maximum Hahn echo coherence time  $T_2^{\text{echo}}$  is reached at the  $\Phi_{\text{ext}}/\Phi_0 = 0.5$  sweet spot, where the spectrum is first-order insensitive to flux noise (compare with Fig. 3c); we discuss the decoherence budget in Supplementary Section VI. The energy relaxation times  $T_1$  extracted from free decay and from quantum jump traces (Supplementary Section VII) are comparable, which indicates a photon-number-independent energy relaxation, as demonstrated for other grAl fluxonium qubits<sup>42</sup>.

Departing from the behaviour of standard fluxonium qubits using mesoscopic SIS junctions, we observe conspicuous fluctuations of the nanojunction  $E_J$  in gralmonium devices. The bottom row of Fig. 3 summarizes the corresponding changes of the qubit frequency on different timescales. On a timescale faster than single measurements (on the order of milliseconds), the qubit toggles between two frequencies that are  $f_{\text{beating}} = 0.2$  MHz apart, resulting in Ramsey fringes with a beating pattern (Fig. 3d). In addition, on a timescale of minutes, we observe frequency jumps of 1.5 MHz, visible both in Ramsey fringes (Fig. 3d) and in continuous wave spectroscopy (compare with Fig. 2 and Supplementary Section VIII). This finding is supported by a

Lorentzian power spectrum characteristic for random telegraphic noise with switching rate  $\Gamma_{\text{RTN}} = 9.4$  mHz (compare with Supplementary Section IX). Moreover, we observe 10–100 MHz jumps every few days while the sample remains at a cryogenic temperature, and the largest changes occur after thermal cycling (Fig. 3e).

These fluctuations are not entirely surprising if one recalls that the first fluxonium levels at half-flux are determined by tunnelling through the Josephson barrier. The frequency of the first transition can be approximated by the phase slip rate<sup>43</sup>

$$v = \frac{4}{\sqrt{\pi}} (8E_J^3 E_C^x)^{1/4} e^{-\sqrt{8E_J/E_C^x}}. \quad (2)$$

Consequently, the qubit frequency is exponentially sensitive to  $E_J/E_C^x$ , rendering the gralmonium susceptible to microscopic changes in the  $(20 \text{ nm})^3$  volume of the grAl nanojunction and its close vicinity. The spectrum is more sensitive to  $E_J$  changes (right-hand axis of Fig. 3e and Supplementary Section VIII) because  $E_C^x$  is bounded by the value of the interdigitated capacitance  $C_q \approx 0.8$  fF, obtained from finite element simulations. The fact that  $E_J$  and  $E_C^x$  fluctuations appear correlated (compare with Supplementary Section X) indicates that the quasiparticle capacitance of the nanojunction<sup>44</sup>, which we estimate to be in the range of 0.05 fF, plays a visible role in the gralmonium.

The list of possible culprits for the intrinsic nanojunction fluctuations includes, but is not limited to, (1) structural changes, that is, tunnelling crystalline defects, vacancies, interstitial impurities or adsorbed molecules<sup>14</sup>; (2) charge noise due to changes in locally trapped charges via the Aharonov–Casher effect<sup>45</sup>; and (3) paramagnetic defects. Future experiments to discriminate between these candidates could involve a local electric field bias using a gate electrode,

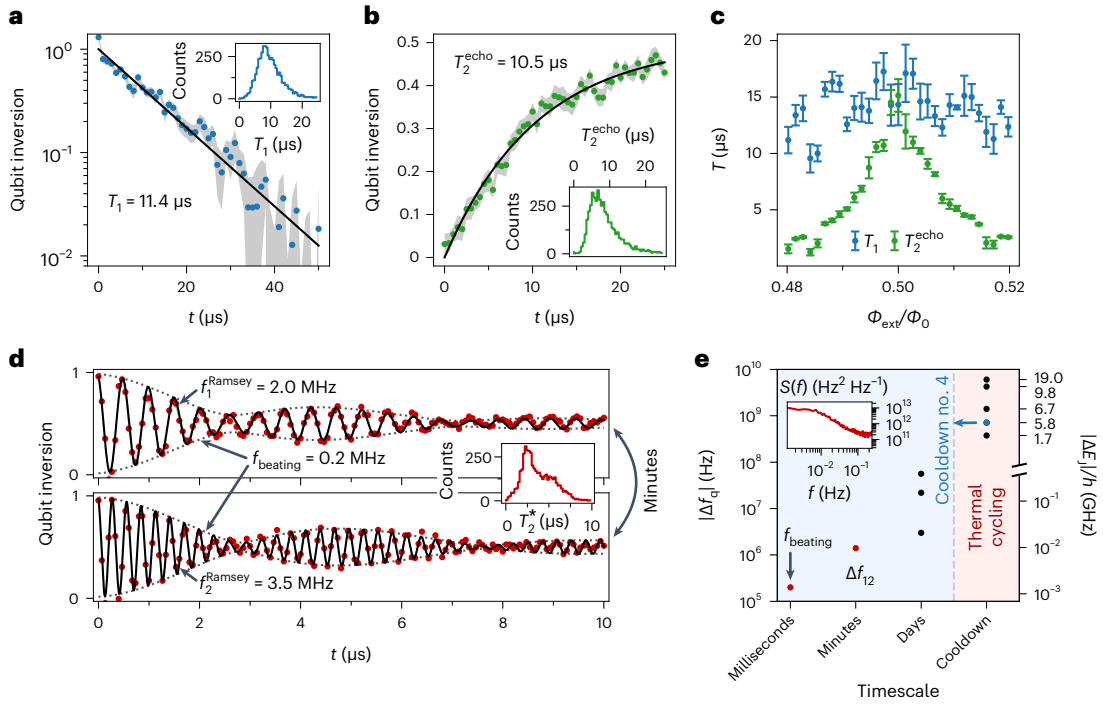


**Fig. 3 | Time domain characterization of the grAlmonium at half-flux bias.**

**a,b,** Free decay energy relaxation **(a)** and spin Hahn echo experiment **(b)** with exponential fits (black lines) corresponding to  $T_1 = 11.4 \mu\text{s}$  and  $T_2^{\text{echo}} = 10.5 \mu\text{s}$ , respectively. **c,** Extracted  $T_1$  and  $T_2^{\text{echo}}$  times  $T$  versus external flux. The markers and error bars represent the mean and standard error of the mean of decay times extracted in five repeated flux sweeps. **d,** Ramsey fringes measured with a nominal detuning of 2 MHz exhibit a beating pattern corresponding to two qubit frequencies separated by  $f_{\text{beating}} = 0.2 \text{ MHz}$  (compare with the two-frequency fit in black and the dotted envelope). Moreover, a comparison of the measurements shown in the top and bottom panels, which were acquired under identical conditions, illustrates jumps of the average qubit frequency by  $\Delta f_{12} = 1.5 \text{ MHz}$  based on the Ramsey fringes frequencies  $f_1^{\text{Ramsey}}$  and  $f_2^{\text{Ramsey}}$ . We fit Ramsey coherence times  $T_2^*$  in the range of 1–10  $\mu\text{s}$  (inset). **e,** We summarize the different timescales on which we observe changes in the qubit frequency. As visible

in **d**, the toggling of the qubit frequency by  $f_{\text{beating}} = 0.2 \text{ MHz}$  occurs on a timescale of milliseconds (Ramsey measurement time) and is accompanied by less frequent jumps of 1.5 MHz on a timescale of minutes (red markers). The inset shows the corresponding Lorentzian power spectrum  $S(f)$  versus frequency  $f$  (see Supplementary Section IX). In addition, we report 10–100 MHz changes every few days during a cooldown. The largest frequency shifts are observed after thermal cycling to room temperature (the cooldown analyzed in detail on faster timescales is marked in blue). The right axis shows the corresponding change of the Josephson energy  $E_j$ , which we identify as the cause of the qubit frequency changes. Note that the measurements in **a–d** are obtained using 20 acquisitions of 100 averaged single-shot qubit measurements; the error bands (grey) show the standard error of the mean over the 20 iterations, and the results of 2,000 individual iterations are histogrammed in the insets.

applying mechanical stress<sup>46</sup> or an in-plane magnetic field. Moreover, the fluctuations might be reduced in future devices by using cold substrate deposition, which has been shown to yield smaller and more regular grains<sup>30</sup>, or post processing such as hydrogen or laser annealing<sup>47</sup>. Beyond detecting changes in its microscopic structure, the nanojunction in a grAlmonium can also be used as a local probe of magnetic field, such as spins in the substrate below the junction, or spin qubits in semiconductors.

In conclusion, we have demonstrated that a grAl nanojunction can provide the source of nonlinearity in a superconducting fluxonium qubit with  $\sim 10 \mu\text{s}$  coherence, enabling its fabrication without the use of mesoscopic JJs, in a single layer of zero-angle deposited grAl. Spectroscopy confirms that the grAlmonium is governed by the standard fluxonium Hamiltonian with a Josephson energy of the grAl nanojunction on the order of those of conventional qubit JJs. In contrast to mesoscopic SIS JJs, the intrinsically small capacitance of the nanojunction,  $C_j < 1 \text{ fF}$ , opens a new parameter regime, particularly relevant for high impedance circuits where large quantum fluctuations of the phase are desirable<sup>18</sup>. Notably, devices such as the  $0-\pi$  qubit biased at half-flux bias would not suffer from  $E_j$  fluctuations of the nanojunctions. Moreover, nanojunctions in which flux tunnelling is suppressed (compare with Supplementary Section II) can be used to replace the overlap JJs in superconducting nonlinear asymmetric inductive elements (SNAILS)<sup>48</sup> for parametric devices.

Beyond grAl, the nanojunction concept presented here can probably be implemented using other granular superconductors<sup>49</sup> or homogeneously disordered superconductors close to the superconducting-to-insulating transition, where the spatial inhomogeneity of the gap creates a structure reminiscent of granular superconductivity<sup>50</sup>.

The nanoscopic footprint of the nonlinear element in the grAlmonium, combined with microsecond coherence times, provides an exciting resource for seemingly antithetic reasons. On one hand, the reduced susceptibility to external magnetic fields enables utilization of the grAl nanojunction in hybrid architectures employing magnetic fields. On the other hand, the increased susceptibility of the nanojunction to microscopic defects and noise channels in its immediate vicinity serves as a sensitive detector and offers a new handle for their characterization. These results open a window of opportunity for material science to directly impact the development of coherent superconducting hardware, with the corresponding nanojunction stability providing an unambiguous metric for improvement.

## References

1. Nakamura, Y., Pashkin, Y. A. & Tsai, J. S. Coherent control of macroscopic quantum states in a single-Cooper-pair box. *Nature* **398**, 786–788 (1999).
2. Koch, J. et al. Charge-insensitive qubit design derived from the Cooper pair box. *Phys. Rev. A* **76**, 042319 (2007).
3. Manucharyan, V. E., Koch, J., Glazman, L. I. & Devoret, M. H. Fluxonium: single Cooper pair circuit free of charge offsets. *Science* **326**, 113–116 (2009).
4. Gu, X., Kockum, A. F., Miranowicz, A., Liu, Y.-x. & Nori, F. Microwave photonics with superconducting quantum circuits. *Phys. Rep.* **718–719**, 1–102 (2017).
5. Blais, A., Grimsmo, A. L., Girvin, S. M. & Wallraff, A. Circuit quantum electrodynamics. *Rev. Mod. Phys.* **93**, 025005 (2021).
6. Kandala, A. et al. Error mitigation extends the computational reach of a noisy quantum processor. *Nature* **567**, 491–495 (2019).
7. Gold, A. et al. Entanglement across separate silicon dies in a modular superconducting qubit device. *npj Quantum Inf.* **7**, 142 (2021).
8. Bao, F. et al. Fluxonium: an alternative qubit platform for high-fidelity operations. *Phys. Rev. Lett.* **129**, 010502 (2022).
9. McEwen, M. et al. Resolving catastrophic error bursts from cosmic rays in large arrays of superconducting qubits. *Nat. Phys.* **18**, 107–111 (2022).
10. Josephson, B. Possible new effects in superconductive tunnelling. *Phys. Lett.* **1**, 251–253 (1962).
11. Kreikebaum, J. M., O'Brien, K. P., Morvan, A. & Siddiqi, I. Improving wafer-scale Josephson junction resistance variation in superconducting quantum coherent circuits. *Supercond. Sci. Technol.* **33**, 06LT02 (2020).
12. Paik, H. et al. Observation of high coherence in Josephson junction qubits measured in a three-dimensional circuit QED architecture. *Phys. Rev. Lett.* **107**, 240501 (2011).
13. Somoroff, A. et al. Millisecond coherence in a superconducting qubit. Preprint at <https://arxiv.org/abs/2103.08578> (2021).
14. Siddiqi, I. Engineering high-coherence superconducting qubits. *Nat. Rev. Mater.* **6**, 875–891 (2021).
15. Krause, J. et al. Magnetic field resilience of three-dimensional transmons with thin-film Al/AlO<sub>x</sub>/Al Josephson junctions approaching 1 T. *Phys. Rev. Appl.* **17**, 034032 (2022).
16. Clerk, A. A., Lehnert, K. W., Bertet, P., Petta, J. R. & Nakamura, Y. Hybrid quantum systems with circuit quantum electrodynamics. *Nat. Phys.* **16**, 257–267 (2020).
17. Kurizki, G. et al. Quantum technologies with hybrid systems. *Proc. Natl Acad. Sci. USA* **112**, 3866–3873 (2015).
18. Groszkowski, P. et al. Coherence properties of the 0- $\pi$  qubit. *New J. Phys.* **20**, 043053 (2018).
19. Peruzzo, M. et al. Geometric superinductance qubits: controlling phase delocalization across a single Josephson junction. *PRX Quantum* **2**, 040341 (2021).
20. Janvier, C. et al. Coherent manipulation of Andreev states in superconducting atomic contacts. *Science* **349**, 1199–1202 (2015).
21. Hays, M. et al. Coherent manipulation of an Andreev spin qubit. *Science* **373**, 430–433 (2021).
22. Pita-Vidal, M. et al. Gate-tunable field-compatible fluxonium. *Phys. Rev. Appl.* **14**, 064038 (2020).
23. Tinkham, M. in *Introduction to Superconductivity* Ch. 6.1 (Dover Publications, 2004).
24. Golubov, A. A., Kupriyanov, M. Y. & Il'ichev, E. The current-phase relation in Josephson junctions. *Rev. Mod. Phys.* **76**, 411–469 (2004).
25. Lam, S. K. H. Noise properties of SQUIDs made from nanobridges. *Supercond. Sci. Technol.* **19**, 963–967 (2006).
26. Astafiev, O. V. et al. Coherent quantum phase slip. *Nature* **484**, 355–358 (2012).
27. Peltonen, J. T. et al. Coherent dynamics and decoherence in a superconducting weak link. *Phys. Rev. B* **94**, 180508 (2016).
28. Grünhaupt, L. et al. Granular aluminium as a superconducting material for high-impedance quantum circuits. *Nat. Mater.* **18**, 816–819 (2019).
29. Zhang, H. et al. Universal fast-flux control of a coherent, low-frequency qubit. *Phys. Rev. X* **11**, 011010 (2021).
30. Deutscher, G., Fenichel, H., Gershenson, M., Grünbaum, E. & Ovadyahu, Z. Transition to zero dimensionality in granular aluminum superconducting films. *J. Low Temp. Phys.* **10**, 231–243 (1973).
31. Glezer Moshe, A., Farber, E. & Deutscher, G. Granular superconductors for high kinetic inductance and low loss quantum devices. *Appl. Phys. Lett.* **117**, 062601 (2020).
32. Borisov, K. et al. Superconducting granular aluminum resonators resilient to magnetic fields up to 1 tesla. *Appl. Phys. Lett.* **117**, 120502 (2020).
33. Kou, A. et al. Simultaneous monitoring of fluxonium qubits in a waveguide. *Phys. Rev. Appl.* **9**, 064022 (2018).
34. Cohen, R. W. & Abeles, B. Superconductivity in granular aluminum films. *Phys. Rev.* **168**, 444–450 (1968).
35. Voss, J. N. et al. Eliminating quantum phase slips in superconducting nanowires. *ACS Nano* **15**, 4108–4114 (2021).
36. Maleeva, N. et al. Circuit quantum electrodynamics of granular aluminum resonators. *Nat. Commun.* **9**, 3889 (2018).
37. Levy-Bertrand, F. et al. Electrodynamics of granular aluminum from superconductor to insulator: observation of collective superconducting modes. *Phys. Rev. B* **99**, 094506 (2019).
38. Winkel, P. et al. Nondegenerate parametric amplifiers based on dispersion-engineered Josephson-junction arrays. *Phys. Rev. Appl.* **13**, 024015 (2020).
39. Smith, W. C. et al. Quantization of inductively shunted superconducting circuits. *Phys. Rev. B* **94**, 144507 (2016).
40. Friedrich, F. et al. Onset of phase diffusion in high kinetic inductance granular aluminum micro-SQUIDs. *Supercond. Sci. Technol.* **32**, 125008 (2019).
41. Winkel, P. et al. Implementation of a transmon qubit using superconducting granular aluminum. *Phys. Rev. X* **10**, 031032 (2020).
42. Gusenkova, D. et al. Quantum nondemolition dispersive readout of a superconducting artificial atom using large photon numbers. *Phys. Rev. Appl.* **15**, 064030 (2021).
43. Rastelli, G., Pop, I. M. & Hekking, F. W. J. Quantum phase slips in Josephson junction rings. *Phys. Rev. B* **87**, 174513 (2013).
44. Eckern, U., Schön, G. & Ambegaokar, V. Quantum dynamics of a superconducting tunnel junction. *Phys. Rev. B* **30**, 6419–6431 (1984).
45. Pop, I. M. et al. Experimental demonstration of Aharonov-Casher interference in a Josephson junction circuit. *Phys. Rev. B* **85**, 094503 (2012).
46. Lisenfeld, J. et al. Electric field spectroscopy of material defects in transmon qubits. *npj Quantum Inf.* **5**, 105 (2019).
47. Hertzberg, J. B. et al. Laser-annealing Josephson junctions for yielding scaled-up superconducting quantum processors. *npj Quantum Inf.* **7**, 129 (2021).
48. Frattini, N. E. et al. 3-wave mixing Josephson dipole element. *Appl. Phys. Lett.* **110**, 222603 (2017).

49. Beloborodov, I. S., Lopatin, A. V., Vinokur, V. M. & Efetov, K. B. Granular electronic systems. *Rev. Mod. Phys.* **79**, 469–518 (2007).
50. Sacépé, B., Feigel'man, M. & Klapwijk, T. M. Quantum breakdown of superconductivity in low-dimensional materials. *Nat. Phys.* **16**, 734–746 (2020).

## Methods

All samples discussed in this manuscript are fabricated on C-plane, double-side-polished sapphire substrates using lift-off electron-beam lithography. A bilayer resist stack of 700–800 nm methyl methacrylate EL-13 and 300 nm polymethyl methacrylate A4, and a 10 nm chromium anti-static layer is used for writing with a 100 keV electron-beam writer. The structures are developed in a spray developer with a methylisobutyl ketone and isopropanol mixture with a volume ratio of 1:3. Before the metal deposition in a PreVac evaporation system, the substrate is cleaned with a Kaufmann ion source in an Ar/O<sub>2</sub> descum process, and the vacuum is improved using titanium gettering. The 20-nm-thick granular aluminium film is deposited under zero angle, at room temperature and a deposition rate around  $-1 \text{ nm s}^{-1}$  in a dynamic oxygen atmosphere resulting in a chamber pressure of  $10^{-5}$ – $10^{-4}$  mbar. The sheet resistance for the main text sample is  $1.5 \text{ k}\Omega \square^{-1}$ .

## Data availability

All relevant data are available from the corresponding authors upon reasonable request.

## Acknowledgements

We are grateful to U. Vool for fruitful discussions, and we acknowledge technical support from S. Diewald, A. Eberhardt, M. K. Gamer, A. Lukashenko and L. Radtke. Funding is provided by the Alexander von Humboldt Foundation in the framework of a Sofja Kovalevskaja award endowed by the German Federal Ministry of Education and Research and by the European Union's Horizon 2020 programme under grant no. 899561 (AVaQus). P.P. and I.M.P. acknowledge support from the German Ministry of Education and Research within the QUANTERA project SiUCs (FKZ, 13N15209). D.R., S.G., P.W. and W.W. acknowledge support from the European Research Council advanced grant

MoQuOS (no. 741276). Facility use was supported by the Karlsruhe Nano Micro Facility and KIT Nanostructure Service Laboratory. We acknowledge qKit for providing a convenient measurement software framework.

## Author contributions

D.R., S.G., M.S. and I.M.P. conceived and designed the experiment. D.R. and S.G. performed the microwave simulation. P.P., L.H., J.K.H. and A.B. contributed to the device fabrication. D.R., S.G., M.S. and P.W. participated in the measurements. D.R. and S.G. analysed the data. D.R. and S.G. led the paper writing, and M.S., P.P., P.W., J.K.H., W.W. and I.M.P. contributed to the text. W.W. and I.M.P. supervised the project.

## Competing interests

The authors declare no competing interests.

## Additional information

**Correspondence and requests for materials** should be addressed to D. Rieger or I. M. Pop.